Materials Characterization 189 (2022) 111943

Contents lists available at ScienceDirect

Materials Characterization

journal homepage: www.elsevier.com/locate/matchar

Site-specific preparation of plan-view samples with large field of view for atomic resolution STEM and TEM studies of rapidly solidified multi-phase Al—Cu thin films

B. Vishwanadh [a,c,d], Jaehyuk Jo [a], Cecile S. Bonifacio [b], Jörg M.K. Wiezorek [a,*]

[a] Department of Mechanical Engineering and Materials Science, University of Pittsburgh, Swanson School of Engineering, 636 Benedum Hall, 3700 O'Hara Street, Pittsburgh, PA 15261, USA
[b] E.A. Fischione Instruments Inc., 9003 Corporate Circle, Export, PA 15632, USA
[c] Materials Science Division, Bhabha Atomic Research Centre, Trombay, Mumbai 400085, India
[d] Homi Bhabha National Institute, Training School Complex, Anushakti Nagar, Mumbai 400094, India

ARTICLE INFO

Keywords:
Microstructure
TEM
Thin films
Sample preparation
Rapid solidification
Al—Cu alloys

ABSTRACT

The present work describes application of a method for site-specific plan-view sample preparation for atomic column resolution scanning transmission and transmission electron microscopy (STEM and TEM) from free-standing thin films of multi-phase Al-alloys after laser irradiation induced rapid solidification (RS). The electron-transparent multilayer thin film samples (amorphous Si_3N_4 substrate plus metal alloy layer) had a total initial thickness of ≈ 130–200 nm. At such large total sample thickness frequently multiple grains of the same or different phases overlap along the electron beam path in the RS microstructures of the alloys. Consequently, accurate atomic resolution images in TEM and STEM mode, and composition sensitive analytical data of the metastable microstructural features presenting in the RS microstructures cannot be obtained with confidence. Using low-energy concentrated Ar ion beam milling, locally thinned regions with thickness of 20–30 nm with large fields of view ≥ $(30\ \mu m)^2$ suitable for high-resolution TEM/STEM studies have been created with micron-scale site-specificity. As example application, atomic scale resolution TEM/STEM imaging has been performed of the banded grain regions of the RS microstructure established in multi-phase Al—Cu alloy thin films. The sample preparation strategy described here appears to be readily applicable to freestanding thin film specimens in general.

1. Introduction

During liquid-solid processing by electron- and laser-beams, e.g., in additive manufacturing and joining, as well as by melt-spinning and thermal spray deposition, the microstructures of metallic materials typically develop in the initial step by rapid solidification (RS) [1]. The details of the alloy RS microstructures sensitively depend on the conditions at the solidification interface, which are driven far away from equilibrium as large cooling rates, typically in the range of 10^3 to 10^6 K/s, result in interface migration at velocity of up to $\approx 10^2$ m/s [2,3]. RS microstructures in alloys are characterized by scale refinement of the primary and secondary solidification products, formation of metastable phases, and solute concentrations well beyond the respective equilibrium solid solubility limits [1–3]. For alloy dependent large supercritical solidification interface velocity, multi-phase alloys can solidify as a single phase due to the effective suppression of solute partitioning, and even amorphous solids can result [4–6]. Establishing a scientifically sound, physical insight and mechanism informed understanding of microstructure evolution during RS of multi-component alloys is desirable to fully develop the potential of RS processing technologies.

A key metric in theoretical and model descriptions of RS alloy microstructure formation, such as the continuous growth model (CGM) and local non-equilibrium model (LNM), is the solid-liquid interface velocity, v_{SL} [7,8]. Using a unique experimental platform, the Movie-Mode Dynamic Transmission Electron Microscope (MM-DTEM), for in-situ transmission electron microscopy (TEM) has facilitated measurements of the changes in solid-liquid interface velocity during RS in metals and alloys by direct observation of the motion of the solidification interface after laser irradiation [9–16]. For Al and hypoeutectic Al—Cu alloys composition dependent critical velocities of the solid-

* Corresponding author.
E-mail addresses: jaj109@pitt.edu (J. Jo), cs_bonifacio@fischione.com (C.S. Bonifacio), wiezorek@pitt.edu (J.M.K. Wiezorek).

https://doi.org/10.1016/j.matchar.2022.111943
Received 8 February 2022; Received in revised form 29 April 2022; Accepted 3 May 2022
Available online 6 May 2022

liquid interface for characteristic crystal growth mode changes have been reported [10–12,14–16]. Combination of MM-DTEM in situ experiments with quantitative post-mortem analytical scanning transmission and transmission electron microscopy (S/TEM) studies can therefore deliver metrics that are uniquely suitable for validation and evaluation of theoretical and computational model predictions of RS microstructure evolution [14–18].

After laser melting the RS microstructures of hypoeutectic Al—Cu thin films exhibit four distinct morphological regions, which develop for increasing solid-liquid interface velocity: 1) a heat affected zone (HAZ), 2) a transition zone, 3) a cellular growth zone with columnar grains, and 4) the banded morphology grain zone [e.g.,16]. The changes in the RS microstructure morphology are associated with changes in crystal growth modes, which occur for critical values of the solid-liquid interface velocity, v_{SL} [e.g.,19]. Details of the RS microstructure of the HAZ, the transition zone and the cellular growth zone in Al—Cu alloys have been reported previously [10,14]. The HAZ and the transition zone are comprised of α-Al grains and intergranular θ-Al_2Cu phase. The cellular growth zone exhibits columnar morphology grains, which are comprised of an α-Al matrix that contains nanoscale intragranular Al_2Cu phases. Notably, discontinuously distributed intergranular secondary phase in the columnar morphology grains has been identified as θ'-Al_2Cu phase, which is metastable with respect to the stable θ-Al_2Cu phase [14]. The banded morphology zone grains contain alternating bands of compositionally partitioned two-phase and unpartioned single-phase regions [16,19]. The microstructure of the partitioned region mimics that of the cellular growth zone with discontinuously distributed θ'-Al_2Cu phase within the α-Al matrix and the single-phase region has been reported as solute supersaturated α-Al phase [e.g.,16]. The θ'-Al_2Cu particles forming in the RS microstructures of Al—Cu alloys have spheroidal morphology. In contrast, meta-stable θ'-Al_2Cu particles forming via precipitation during aging by solid state phase transformation in Al—Cu alloys have plate shape morphology, obey an orientation relationship, $[100]_\alpha \,||\, [100]_{\theta'}$ and $(001)_\alpha \,||\, (001)_{\theta'}$, and develop coherent interface sections [20–22]. Recent research suggested that the single-phase regions of the banded morphology grains in a hypoeutectic Al—Cu alloy may exhibit solute partitioning and possible early stages of metastable Al_2Cu phase formation at length scales on the order of ≈2–3 nm [16,23]. Additional investigations of the banded morphology grains with atomic column resolution are necessary to elucidate possible origins of these characteristic non-equilibrium features of the Al—Cu alloy RS microstructures, which form under conditions at the extremes of the regime for coupled two-phase growth [6–8,10].

Previous studies of the RS microstructures formed during in-situ MM-DTEM experiments have been limited to mostly nano-scale resolution imaging and analysis [10–15]. The lack of atomic resolution imaging can be attributed to limitations imposed on the thin film specimen geometry for successfully performing the in-situ MM-DTEM observation of alloy RS after pulsed laser irradiation. The typical thin film specimens used for the alloy RS experiments in the MM-DTEM utilized commercially available Pelco™ Silicon Nitride supports (Ted Pella Inc., USA) with a 500 μm by 500 μm electron-transparent window as substrates for deposition of the Al-alloy thin film layer (Fig. 1a). These substrates are nominally ≈ 200 μm thick Si disks of 3 mm diameter covered by a nominally ≈50 nm thick amorphous Si_3N_4 membrane on top of which metal or alloy layers between ≈80 nm to ≈160 nm thick have been deposited by electron beam evaporation or magnetron sputtering [10–16]. The total thickness of the resulting multilayer thin film alloy specimens in the electron-transparent central region is therefore ≈130–210 nm (Fig. 1a and Fig. 1b). Successfully acquiring reliable atomic column resolution images while using S/TEM instruments operating at 100–300 kV acceleration voltage requires reduced

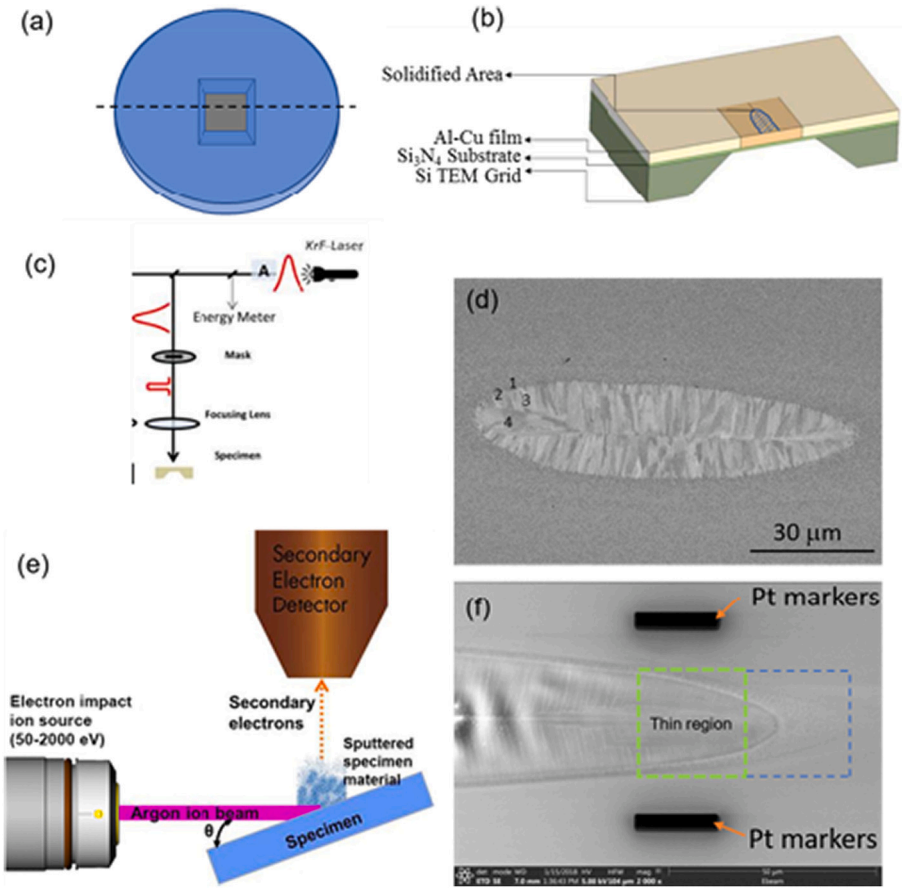

Fig. 1. (a) Schematic of (a) backside view of TEM grid with amorphous Si_3N_4 membrane visible in electron-transparent square window, (b) cross-sectional view of the TEM grid showing Si, Si_3N_4 and AlCu layers from bottom to top, (c) schematic of the laser melting set up, (d) SEM micrograph of a rapidly solidified AlCu alloy melt pool (it consists of four microstructural zones: 1) HAZ, 2) Transition zone, 3) Columnar Zone and 4) Banded region), (e) schematic of the low-energy concentrated Ar ion milling instrument and the TEM sample, and (f) SEM micrograph showing the melt pool and Pt markers for locating the region of interest for ion milling. The area marked by the green dashed-line square was targeted for site-specific Ar ion milling using the scanned ≈1 μm diameter ion beam. While not specifically targeted by the scanned Ar ion beam, the adjacent area marked by the blue dashed-line square also exhibited some thinning. (For interpretation of the references to colour in this figure legend, the reader is referred to the web version of this article.)

thickness in the locations of the electron transparent window where the application of pulsed laser irradiation produced the RS microstructure.

There are several challenges involved in reducing the thickness of the film specimens in the electron transparent regions of interest using conventional sample preparation techniques. Traditional back-thinning from the substrate side to remove the amorphous Si_3N_4 support membrane prior to thinning of the alloy layer with combinations of dimpling and subsequent broad beam Ar ion-milling cannot be applied. Dimpling is ruled out due to the presence of the electron-transparent window. Removal of the amorphous Si_3N_4 layer by ion milling needs to be performed from the backside of the Pelco Silicon Nitride TEM grid (Fig. 1a and Fig. 1b). Unfortunately, the TEM grid geometry and dimensions make it impossible to access the back side of the film at the central region using broad beam ion-milling without milling the Si substrate. Line of sight issues, shadowing and contamination problems prevent the use of broad beam Ar ion-milling approaches to achieve the required site-specific thinning of the thin film alloy in regions of interest located in the electron transparent window. The use of standard focused ion beam (FIB) TEM lift-out methods for excising thin lamellae from the respective regions of interest within the RS microstructures is also problematic [24]. The membrane supported thin films are intrinsically in a stressed state and fragile. This is further exacerbated after rapid thermo-mechanical cycling associated with pulsed laser irradiation induced melting and re-solidification. The required ion-beam cutting and removal of thin film material during standard FIB preparation of thin cross-sectional TEM lamellae exposes the film in the windowed region to high risk of subsequent rupture, tearing and thus loss of the entire sample. Furthermore, large areas of RS microstructure formed in the electron-transparent window of a thin film specimen are destroyed, critically modified by ion irradiation damage or contaminated during the standard FIB preparation to yield a typical ≈100 nm thin and ≈3–10 μm long cross-sectional TEM lamellae with a width approximately equivalent to the multilayer thin film thickness (≈130–210 nm). Thus, for each thin film specimen only small fractions of the RS microstructure can be examined at high resolution when using standard FIB TEM lift-out lamellae preparation. Furthermore, the resulting FIB lift-outs have geometries that render them extremely delicate, fragile, and prone to bending due to thin film stress release. Finally, Al-alloys are prone to develop ion-beam damage related artifacts when Ga-ions are used for FIB-lift-out sample preparation, including ion implantation and undesirable alteration of the sample microstructure [25–27]. Specifically, Ga diffusion to Al grain boundaries at room temperature resulting in liquid embrittlement during FIB preparation is problematic [28,29]. Issues associated with ion-beam modification are critical and must be avoided to successfully study the metastable RS microstructures of the Al—Cu thin films. Therefore, site specific thinning of select regions within the electron transparent window without introduction of damaging artifacts and yielding areas of field-of-view that reliably span multiple grains presenting in the morphologically complex Al-alloy RS microstructure is of prime interest. The benefit of low-energy (≤1 keV) inert gas ion milling by Ar for reducing the effects of surface deposits and ion irradiation damage has been recognized in numerous prior studies [30–33]. Ar is an inert gas that does not react to form chemical bonds with the specimen atoms. Particularly for Al alloys, Ar ion milling effectively removes Ga implanted layers induced by Ga ion FIB preparation by the reduction of chemical potential of Ga on the surface, effecting the outward diffusion of Ga away from the grain boundaries [26]. The current work describes a robust procedure for preparation of plan-view specimens from thin films deposited on commercially available windowed TEM grid sample supports that delivers large fields of view suitable for atomic resolution S/TEM imaging and analysis. The specimen preparation procedure utilizes select capabilities offered by dual-beam FIB instruments and low-energy concentrated ion beam (CIB) Ar milling [34]. As example application, atomic scale resolution TEM and STEM imaging of the banded grain regions of the RS microstructure established in a multi-phase Al—Cu alloy during in-situ MM-DTEM experiments have been performed.

2. Experimental Procedures

Binary thin film alloy samples of Al—Cu have been obtained by depositing pure Al and Cu metal using electron beam evaporation on the amorphous Si_3N_4 membrane of square window Si TEM grids (Fig. 1a and Fig. 1b). The thickness of the deposited Al—Cu alloy film has been determined by surface profilometer measurements ≈ 140 nm. The total thickness of the electron transparent region of the specimens including the amorphous Si_3N_4 membrane is therefore estimated as ≈ 190 nm (Fig. 1b). To obtain rapid solidification (RS) microstructures, several locations within the electron transparent 500 μm by 500 μm square window region in the center of the TEM grid specimens of the deposited Al—Cu thin film have been irradiated with a single 248 nm (KrF) excimer laser pulse of 15 ns duration. Projecting the central region of the circular cross-section laser beam through a single-slit Cu-mask with approximately rectangular shape and aspect ratio of side-lengths of about 1:8 to 1:10 followed by a ten-fold times demagnification focusing lens permitted control of the shape and dimensions of the laser beam at the specimen and thus of the shape and size of the resulting melt pool (Fig. 1c). A small central part of the laser beam emitted by the KrF-excimer system was selected with the mask to obtain an approximately top-hat laser profile for the irradiated regions on the thin film alloy specimens [2,3]. The energy and geometry of the laser pulse was configured to initiate complete melting of the Al—Cu alloy layer without destroying the nanoscale thin film multilayer in the electron transparent window of the TEM grid sample. Successful pulsed laser irradiation resulted in melt pools of elongated elliptical shapes with dimensions in the range of approximately 23–35 μm wide and 120–230 μm long. After application of the laser pulse, the alloy layer first melts to form a pool of liquid bordered laterally by solid alloy thin film and supported by the nitride membrane, which is transparent to the laser irradiation and remains solid. The melt pool subsequently starts to cool, primarily by heat conduction through the thin metal alloy layer, and alloy solidification is accomplished via directional solidification and epitaxial growth from the melt pool perimeter towards its center [e.g.,10–12]. The essential elements of the ex-situ laser system used here for Al—Cu thin film RS experiments are shown schematically in Fig. 1c. Fig. 1d shows an example of the RS microstructure established from the pulsed laser irradiation induced alloy melt pool. The four morphologically distinct microstructural zones characteristic of the RS microstructure of hypo-eutectic Al—Cu alloys can be discerned (see markers 1, 2, 3 and 4 in Fig. 1d) [e.g.,10].

A low-energy concentrated ion beam (CIB) Ar milling instrument (Model 1040 NanoMill® TEM specimen preparation system, E.A. Fischione Instruments) with a micron-scale ion beam and beam scanning capability was used for site-specific specimen thickness reduction. Subsequently, atomic resolution imaging of the morphologically different areas that evolved during RS of the alloy thin film was performed. Fig. 1e schematically depicts the Ar ion-beam with a diameter of about 1 μm at low-energy (<2 keV) targeted within an area of the TEM grid specimen that is tilted (tilt range = +30° to −10°). The specimen thickness is reduced by the concentrated Ar ion beam moving in a raster pattern across a user-specified area of the electron transparent window of the TEM grid by sputtering processes. Prior to low-energy CIB Ar milling, electron beam stimulated deposition of fiducial Pt markers was performed on the amorphous Si_3N_4 membrane layer using a dual-beam focused ion beam (DB-FIB) instrument (Scios, Thermo Fisher) to mark the area of interest. The fiducial markers facilitated reliable targeting of the region of interest on the thin film (Fig. 1(f)) during CIB Ar milling. The specimen was tilted to +30° to target the region of interest located within the 500 μm by 500 μm square window of the TEM grid specimen from the back-side to remove the amorphous Si_3N_4 membrane layer prior to subsequent thinning of the alloy layer locally. The CIB Ar milling was performed at 900 eV accelerating potential with a beam current of

100 pA for a nominal (30 μm × 30 μm) target size box (e.g., green box in Fig. 1f). After ion milling for 7 h, areas as large as (40 μm × 40 μm) were suitable for atomic resolution imaging. The blue box marked in Fig. 1f delineates an area adjacent to the nominally selected target area, which exhibited minor signs of ion-beam thinning.

S/TEM imaging and analysis were performed using a Tecnai G2 F20 UT (Thermo Fisher) operated in TEM mode and an aberration-corrected Titan Themis G2 200 Cs (Thermo Fisher) operated in STEM mode at 200 kV. The thickness of the specimens prior to and after the scanned microbeam low-energy Ar ion milling was measured using energy-filtered TEM (EFTEM) imaging techniques through electron energy loss spectroscopy (EELS) with a Gatan Imaging Filter (GIF) system (Gatan, Inc.) attached to a Tecnai TF30 (Thermo Fisher) TEM operated at 300 kV [35].

3. Results and Discussion

Fig. 2. shows examples of phase contrast high-resolution TEM (HREM) images of the θ'-Al_2Cu phase particles embedded in the α-Al matrix before CIB Ar milling. These particles were observed in the two-phase bands of the banded morphology grains in the RS microstructure (e.g., marker 4 in Fig. 1d) of a Al-11 at.%Cu alloy at the [110] and [001] zone axis orientations. The α-Al matrix and the spheroidal shape θ'-Al_2Cu phase particle can be discerned readily with lattice resolution. However, the presence of Moiré and double-diffraction effects, particularly for the regions associated with the θ'-Al_2Cu particle, renders atomic column resolution studies of the structure of the interface with the α-Al matrix impossible (Fig. 2a and b). Several examples of θ'-Al_2Cu particles were found with the presence of these diffraction related imaging artifacts (See Supplementary Information, Fig. S1 for the TEM images). These undesirable image contrast features are attributed to the overlapping of the θ'-Al_2Cu phase particles and the surrounding α-Al matrix. Image contrast is further affected detrimentally by the presence of the amorphous Si_3N_4 membrane layer. Frequent contrast reversal is typically observed in HREM imaging as the defocus is adjusted. This is intrinsically associated with the highly oscillatory contrast transfer function of the field-emission TEM instruments used here, adding to the complexity of reliable image contrast interpretation. The relative thickness of the thin film alloy specimen was determined by electron energy loss spectroscopy (EELS) by energy-filtered TEM (EFTEM) thickness mapping at 300 KV accelerating voltage. The EFTEM thickness map of the two-phase (TP in Fig. 2c) and single-phase (SP in Fig. 2c) bands of the banded grain region indicates that the specimen thickness is $(t/\lambda) \approx 1.2$ on average and exhibited peaks at $(t/\lambda) \approx 1.4$ (Fig. 2c). Here, t is the thickness of the specimen in the direction of the electron path and λ is the mean free path length for inelastic scattering of the electrons. Considering a combined thickness of 190 nm for the Al plus amorphous Si_3N_4, this implies an effective inelastic electron scattering mean free-path length of $\approx 140\ \text{nm} \leq \lambda \leq \approx 160\ \text{nm}$. This appears reasonable for the 300 keV electrons utilized in the EELS mapping, given the value of $\lambda = 134$ nm reported for 200 KV accelerating voltage in Al [35,36].

Fig. 3a and Fig. 3b show examples of HREM images after CIB Ar milling obtained for the [001] and [110] zone axes orientations of the Al matrix lattice from the partitioned two-phase bands of the banded morphology grains in the RS microstructure of an Al-11 at.% Cu alloy. The undesirable contrast effects of Moiré fringes were absent in the regions entirely associated with the θ'-Al_2Cu phase and the α-Al matrix, respectively (Fig. 3a and b). The overall HREM image quality is improved. The EFTEM thickness map shown in Fig. 3c was obtained after CIB Ar milling the selected area of 40 μm × 40 μm of the α-cells and banded morphology region of the RS microstructure of the Al—11Cu alloy. The inset in Fig. 3a shows an overview of the thinned region, which spans the morphologically distinct zones established in the RS microstructure of the alloy, and the approximate location from which the STEM images were acquired. The average thickness represented by the value of (t/λ) for the banded region grains decreased to $(t/\lambda) \approx 0.2$ (Fig. 3c). This represents a thickness reduction by ≈ 83% (1–(0.2/1.2)) of the original thickness of the combined Al layer and the amorphous Si_3N_4 support membrane. Low-energy CIB Ar milling drastically reduced the absolute magnitude of variations in thickness of the specimen (compare Fig. 2c and Fig. 3c). The specimen after Ar milling produced large fields of view that are approaching the regime of thin foil section thicknesses for which atomic column resolution plan view HREM imaging and atomic resolution high-angle annular dark-field STEM (HAADF STEM) become feasible. Given the mean free path ranging from $\lambda = 140$–160 estimated earlier, the specimen thickness range of $t = (0.20 * 140\ \text{nm}$ to $0.20 * 160) \approx 28$ to 32 nm is calculated. At this thickness, little to no overlap is expected between the α-Al matrix lattice and the discontinuously distributed θ'-Al_2Cu phase particles, which typically exhibit cross-sectional dimensions of 20–40 nm [16,23]. Therefore, the conditions required for Moiré effects are generally not satisfied for the central regions of the θ'-Al_2Cu phase particles permitting structural studies by HREM.

The θ'-Al_2Cu phase particle imaged in projection along [001] in Fig. 3a exhibits relatively flat (200), (020), (110) and $(\bar{1}10)$ facets and approximately equiaxial cross-sectional dimensions of about 22–24 nm. Yellow dashed lines in Fig. 3a delineate the orientations of (200), (020) and (110) planes, respectively, in the vicinity of the coherent (α/θ')-interface sections. The HREM image of Fig. 3a, obtained along the [001] zone axis, clearly demonstrates the presence of coherent interface sections between the α-Al and θ'-Al_2Cu crystals. The (200), (020) planes and (110), $(\bar{1}10)$ planes in the two phases align perfectly. Thus, for the

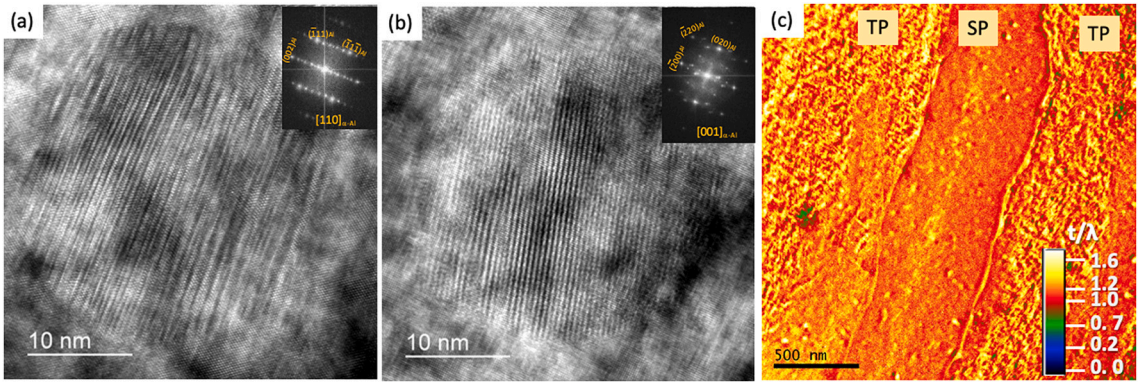

Fig. 2. HREM micrographs along (a) [110] and (b) [001] zone axes of a-Al showing the presence of Moiré effects and fringes in the regions of the θ'-Al_2Cu crystals, insets in (a), (b) show the corresponding diffraction patterns having double diffraction spots, and (c) EELS thickness map, (t/λ), obtained by EFTEM showing the variation of thickness from $t/\lambda \sim 1.2$ to 1.4, where TP and SP mark two-phase and single-phase bands, respectively, of the banded grain. (For interpretation of th references to colour in this figure caption and/or associated text, the reader is referred to the web version of this article).

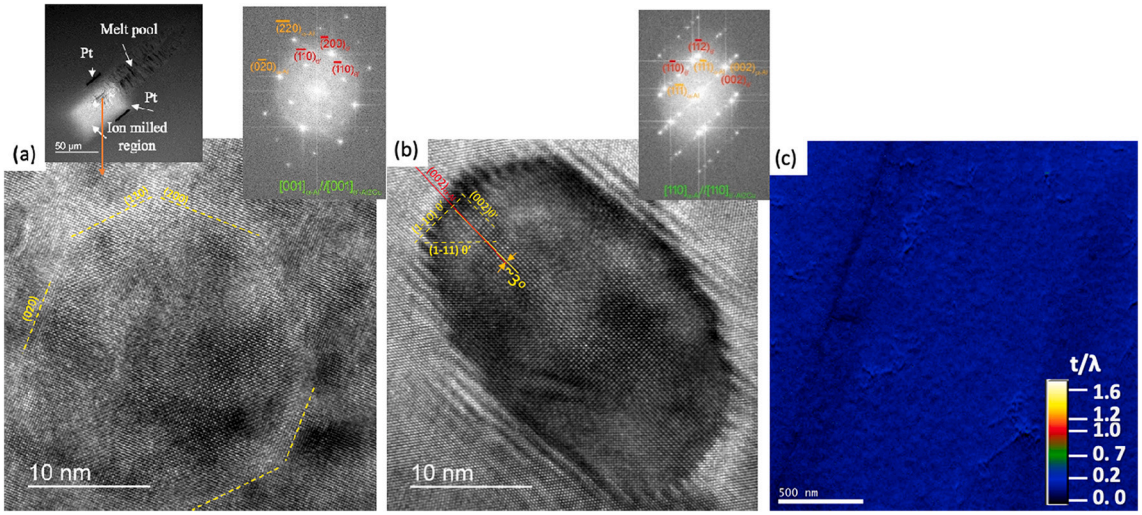

Fig. 3. HREM micrographs along (a) [001] and (b) [110] zone axes after low-energy Ar ion milling on the back side of TEM grid on Si_3N_4 membrane showing atomic resolution image of θ'-Al_2Cu crystals, insets in (a) and (b) show the Fast Fourier Transforms of the HREM images and for (a) also low magnified TEM image of the melt pool which shows the thinned region prepared by site-selective scanned micro-beam Ar ion milling, and (c) EFTEM thickness map, (t/λ), from the thinned region showing uniform thickness of on average (t/λ) ≈ 0.2 (see text for more details). (For interpretation of th references to colour in this figure caption and/or associated text, the reader is referred to the web version of this article).

$(002)_\alpha//(002)_{\theta'}$ segments of the (α/θ')-interface coherent structure results. This is consistent with orientation relationships reported previously for the α-Al and θ'-Al_2Cu phase formed during RS of hypoeutectic Al—Cu alloys [14,16]. HREM images of the θ'-Al_2Cu phase particles obtained for the perpendicular orientation along the [110] zone axis of the Al lattice (e.g., Fig. 3b) reveal relatively flat coherent interface sections associated with the (002) planes, while the other, more prominently curved interfacial segments exhibit a terrace-ledge structure. The terrace-ledge structure can be described by combinations of (002) and $(1\bar{1}0)$ terraces and ledges with respect to the α-Al lattice. Traces and orientations of prominent edge-on oriented planes, e.g., (002), $(1\bar{1}0)$

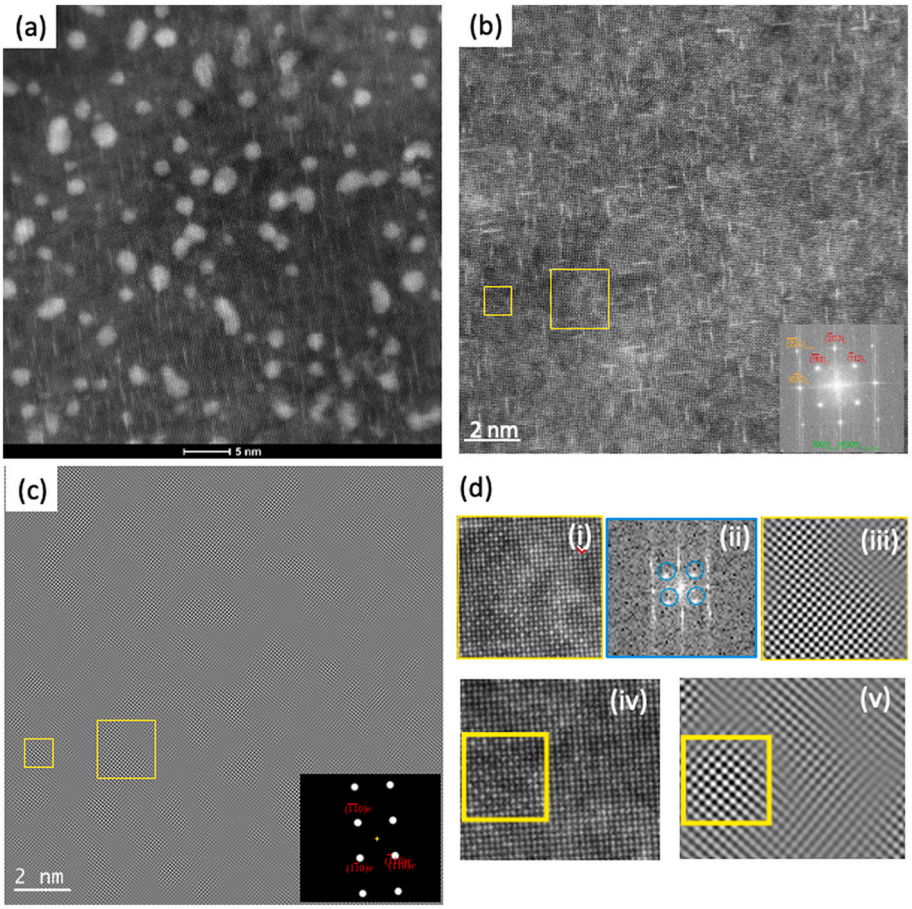

Fig. 4. HAADF STEM images from a single-phase band of the banded region for (a) [110] orientation of Al showing the presence of GP zones as well as Pt rich clusters, (b) for [001] orientation of Al acquired after low energy concentrated Ar ion beam milling from the top-side of the melt pool showing only GP zones, no Pt rich clusters are present with FFT of HAADF image as inset. (c) is inverse FFT of the HAADF image in (b) after filtering with a θ'-phase-specific mask shown as inset in (b) bottom right. The smaller and larger yellow squares mark equivalent regions in (b) and in (c). (d) shows panel (i) and (iii), which are magnified views of the large square region in (b and c), panel (ii) is the FFT for panel (i); panels (iv) and (v) are magnified views of the region around the smaller square marked in (b) and (c) and show the α-Al lattice outside and θ'-phase lattice inside of the yellow square. The bright contrast regions in (c) are associated with θ'-phase chemically ordered structure. (For interpretation of the references to colour in this figure legend, the reader is referred to the web version of this article.)

and $(1\bar{1}1)$, are marked in Fig. 3b for convenience. The cross-sectional dimension of the θ'-Al_2Cu phase particle imaged in Fig. 3b are about 17 nm and 30 nm along the [001] and $[1\bar{1}0]$ directions in the α-Al lattice, respectively. The θ'-Al_2Cu phase particles clearly are of spheroidal shape rather than of plate or disk shape. Disk shape is observed for θ'-Al_2Cu phase in Al alloys after solid-state precipitation due to significant lattice misfit strain effects on interfacial free energy [20–22]. The remaining delocalization and Moiré-effects discernible in HREM images obtained for the [110] zone axis projection (e.g., Fig. 3b) are therefore attributed to the overlap of the α-Al and the spheroidal shape θ'-Al_2Cu phase particles at their perimeter. Further examining the HREM images and fast-Fourier-transform (FFT) of the HREM images obtained for the [110] zone axis projection revealed consistently a relative rotation in the alignments of the (002) planes in the α-Al and θ'-Al_2Cu phases by three degrees. Small but significant deviation from the perfect alignment of the α-Al and θ'-Al_2Cu lattices associated with the orientation relationship described as $[100]_{\alpha} \,||\, [100]_{\theta'}$ and $(001)_{\alpha} \,||\, (001)_{\theta'}$ is further evidence of the non-equilibrium nature of the θ'-Al_2Cu phase particles formed during RS in the Al—Cu alloys, and consistent with conditions that can lead to Moiré effects in phase contrast HREM images (see also Supplementary Information, Fig. S2).

The same sample was also imaged by high-angle annular dark-field (HAADF) STEM. The HAADF image in Fig. 4a obtained from the [110] orientation of the α-Al lattice in a single-phase band of a banded morphology zone grain shows the presence of bright contrast clusters, typically, about 2–4 nm in size. These clusters are comprised of atoms with high atomic number relative to Al, which have been identified as Pt by STEM energy dispersive X-ray spectroscopy (EDS). These clusters exhibit a structure consistent with a face-centered cubic crystal and are coherent with the Al lattice. Additionally, linear contrast features with a contrast level intermediate to that of the darker Al matrix lattice and the brighter Pt clusters are observed to align parallel to the {002} of Al. These features are consistent with edge-on Cu-based Gunnier-Preston (GP) zones that are about 1.4–2.8 nm in diameter. The GP zones formed during the 90+ days of natural aging at room temperature in the laboratory environment that elapsed between the pulsed laser irradiation melting induced RS and the STEM imaging of the banded morphology grains. The Pt presenting in the bright contrast clusters have been introduced unintentionally as a surface artifact by the gas injection system of the FIB instrumentation during the making of Pt fiducial markers, which are important for reliably relocating of the region of interest selected for thickness reduction by CIB Ar milling (e.g., TEM image inset in Fig. 3a). To remove these superficial surface artifacts, CIB Ar milling was carried out for the topside, i.e., the deposition side of the Al—Cu alloy layer, for about half an hour, ≈0.5 h, using 900 eV ion energy. Subsequently, HAADF STEM images only show the presence of GPZ's in the Al lattice, demonstrating the successful removal of the Pt clusters from the thin film surface (e.g., Fig. 4b). The FFT of [001] zone axis orientation from the HAADF images showed the presence of image contrast periodicities that are consistent with the chemical ordering of the Al and Cu layers along the ⟨110⟩ in the tetragonal θ'-Al_2Cu phase (e.g., inset Fig. 4b). For convenience of comparison, two areas exhibiting θ'-Al_2Cu phase in Fig. 4b are marked by squares and highlight equivalent locations in Fig. 4c and Fig. 4d. FFT analysis of these areas showed that the regions inside the squares have a chemically ordered structure consistent with θ'-Al_2Cu phase, while the region between the two squares is associated with the α-Al phase lattice (Fig. 4d, panels (i) to (v)). To enhance the contrast between the dominant α-Al matrix lattice and the regions exhibiting apparent θ'-Al_2Cu structure (e.g., inset of Fig. 4c) an inverse FFT has been generated after applying a mask to select only the chemical ordering related image frequencies specifically for the $(110)_{\theta'}$. The resulting inverse FFT reveals as brighter contrast features θ'-Al_2Cu ordered regions with characteristic dimensions of about 1–2 nm across embedded within the α-Al grain of the banded region (Fig. 4f). This indicates that elemental partitioning in the diffusion boundary layer of liquid alloy adjacent to the growing solid crystal is still feasible at limited spatial scales of up to ≈ 1–2 nm. Prior reports proposed that these nm-scale regions of chemically ordered structure in the single-phase bands of the banded morphology grains of the RS microstructure of the Al-11 at.%Cu alloy are sub-critically sized embryos of θ'-Al_2Cu [16,23].

The sample preparation method presented here enabled atomic resolution STEM/TEM studies of the structure and composition of the metastable features characteristic of the RS microstructure established after PL irradiation induced melting in multi-phase Al—Cu thin films. The method combines the use of dual-beam FIB instrumentation for electron-beam stimulated Pt deposition of fiducial markers with CIB Ar milling to reliably provide large fields of view of locally thinned regions, e.g., ≈30 μm by ≈30 μm in Fig. 1f, suitable for accurate high-resolution STEM/TEM imaging and analysis. Fabricating the Pt fiducial markers is critically important for reproducibly and confidently re-locating of the regions of interest for site-specific thinning by the micrometer diameter low-energy Ar ion beam. Images obtained with the secondary electron detector of the CIB Ar-milling instrument rely on the high-contrast provided by the Pt markers relative to the Al-alloy to accurately target the region of interest for site-specific thinning. To evaluate the thinning progress of the Ar ion-milling, the specimens have been examined iteratively by TEM. Alternatively, SEM imaging can be utilized for this purpose. The rate of material removal during the low-energy CIB Ar milling performed here (900 eV ion energy, 100 pA ion current, at +30° sample tilt) has been estimated as ≈ 0.4 nm/min, i.e., ≈ 158 nm over 7 h. This relatively low milling rate is related to the scanning of the micrometer diameter CIB across a large target area of 30 × 30 μm^2. The present method avoided exposing the Al alloy to Ga ion irradiation damage and formation of associated artifacts in the non-equilibrium microstructures resulting from RS of the nanoscale alloy thin film layer. Furthermore, the large-field of view, up to about ≈$(50\ \mu m)^2$ (e.g., inset of Fig. 3a), available for plan-view geometry atomic resolution STEM/TEM studies spans the four morphologically distinct regions developing in the RS microstructures of the Al alloy. This facilitates comparisons of the structure and composition of the characteristic features formed in the RS microstructure as the solid-liquid interface velocity changes using one specimen [e.g.,16]. Thus, in comparison to conventional broad beam Ar ion milling and TEM FIB lift-out sample preparation the present method offers unique advantages. For example, the selected site of interest can be thinned to the required thickness without imparting significant damage or irreversible artifacts to the remainder of the free-standing membrane window of the TEM grid supported specimens used here for the study of RS microstructure evolution in Al—Cu alloys. This is not the case for TEM FIB lift-out sample preparation. When using Ga ions modifications of the metastable RS microstructure by ion implantation and ion beam damage are prone to introduce crystal defects or facilitate other irreversible microstructural changes. This complicates or prevents reliable examination of the metastable features formed during alloy RS. Furthermore, only very small areas of the RS microstructure with its spatially varying morphology (e.g., up to 10 μm by 0.1 μm in the plane of the thin film) can be examined in a single TEM FIB lift-out sample, while damaging or destroying larger areas adjacent to the selected site for sample extraction from the thin film. The approach of applying fiducial markers to enable efficient successful targeting of a local area of interest offers potential for adoption to perform site-specific thinning with the low-energy CIB Ar milling for thin film specimens in general, and even when using conventional 3 mm diameter thin disk TEM specimens prepared by electropolishing [e.g.,37] and/or dimpling.

4. Summary and Conclusions

A reliable method for preparation of samples suitable for obtaining atomic resolution STEM/TEM images from rapidly solidified multiphase Al—Cu thin films has been described. The method uses electron

imaging and electron beam assisted Pt deposition in a dual-beam FIB instrument for fabrication of fiducial markers and low-energy concentrated Ar ion beam milling for site-specific specimen thickness reduction. In comparison to methods using conventional broad beam ion milling and FIB preparation of TEM lift-out lamellae, the present method offers advantages for preparing site-specific large fields of view with areal dimension on the order of $\approx 1000\ \mu m^2$ that are artifact free, while avoiding damaging the remaining area of the sample. The sample preparation method can be utilized to prepare thin regions from any kind of freestanding thin film specimens and may even offer potential for site-specific thinning of local areas of conventional 3-mm diameter TEM disk samples obtained by electrochemical-polishing. After application of the sample preparation method described here high-resolution images from the banded region of rapidly solidified Al—Cu thin films have been obtained successfully. The reduction in specimen thickness from the range of originally about 200 nm to about 20–30 nm suppressed or even fully removed detrimental Moiré and possible double diffraction effects which originally prevented accurate and reliable interpretation of HREM images of metastable features of the RS alloy microstructure. The plan-view HREM and STEM studies performed after the local site-specific specimen thickness reduction revealed crystal lattice level details of the structure of metastable θ'-Al_2Cu phase formed during RS. The study shows that the sample preparation method described here uniquely facilitated atomic level studies that benefit experimental research of the evolution of multiphase microstructures during RS of multicomponent alloys, which in turn provides data suitable for the evaluation and validation of predictions from complementary computational modeling of microstructure formation in laser-melting facilitated additive manufacturing.

Conflicts Competing Interest Individual contributions

Individual contributions to the research and the article:

The manuscript was written through contributions of all authors. VB and CSB prepared the first original draft manuscript. VB, CSB, JJ and JMKW edited and prepared the final manuscript. All authors have read the manuscript and agreed to the published version. VB performed Ar ion milling, TEM, STEM analysis, other characterization of the rapidly solidified alloy specimens, data curation and analysis. JJ performed the dual-beam FIB operation and associated imaging, data curation and analysis. CSB assisted in Ar ion milling sample preparation and performed EFTEM maps acquisition. JMKW performed the pulsed laser melting of the thin film specimens, analyzed and interpreted the data. JMKW conceptualized, administered, and secured the funding for the research project.

Declaration of Competing interest

The authors declare that they have no known competing financial interests or personal relationships that could have appeared to influence the work reported in this paper.

Acknowledgements

This research received support from the National Science Foundation, Division of Materials Research, Metals & Metallic Nanostructures program through Grant No. DMR 1607922.

Appendix A. Supplementary data

Supplementary data to this article can be found online at https://doi.org/10.1016/j.matchar.2022.111943.

References

[1] E.J. Lavernia, T.S. Srivatsan, The rapid solidification processing of materials: science, principles, technology, advances, and applications, J. Mater. Sci. 452 (45) (2009) 287–325, https://doi.org/10.1007/S10853-009-3995-5, 2010.
[2] R. Zhong, A. Kulovits, J.M.K. Wiezorek, J.P. Leonard, Four-zone solidification microstructure formed by laser melting of copper thin films, Appl. Surf. Sci. 256 (2009) 105–111, https://doi.org/10.1016/j.apsusc.2009.07.084.
[3] A. Kulovits, R. Zhong, J.M.K. Wiezorek, J.P. Leonard, Electron microscopy of geometrically confined copper thin films after rapid lateral solidification, Thin Solid Films 517 (2009) 3629–3634, https://doi.org/10.1016/j.tsf.2008.11.132.
[4] H. Kimura, A. Inoue, S. Yamaura, K. Sasamori, M. Nishida, Y. Shinpo, H. Okouchi, Thermal stability and mechanical properties of glassy and amorphous Ni-Nb-Zr alloys produced by rapid solidification, Mater. Trans. 44 (2003) 1167–1171, https://doi.org/10.2320/matertrans.44.1167.
[5] W. Kurz, D.J. Fisher, Fundamentals of Solidification, Fourth Rev, Trans Tech Publications, Zurich, Switzerland, 1998.
[6] W. Kurz, B. Giovanola, R. Trivedi, Theory of microstructural development during rapid solidification, Acta Metall. 34 (1986) 823–830, https://doi.org/10.1016/0001-6160(86)90056-8.
[7] M.J. Aziz, T. Kaplan, Continuous growth model for interface motion during alloy solidification, Acta Metall. 36 (1988) 2335–2347, https://doi.org/10.1016/0001-6160(88)90333-1.
[8] P. Galenko, S. Sobolev, Local nonequilibrium effect on undercooling in rapid solidification of alloys, Phys. Rev. E 55 (1997) 343–352, https://doi.org/10.1103/PhysRevE.55.343.
[9] T. LaGrange, B.W. Reed, M.K. Santala, J.T. McKeown, A. Kulovits, J.M. K. Wiezorek, L. Nikolova, F. Rosei, B.J. Siwick, G.H. Campbell, Approaches for ultrafast imaging of transient materials processes in the transmission electron microscope, Micron. 43 (2012) 1108–1120, https://doi.org/10.1016/j.micron.2012.04.010.
[10] J.T. McKeown, A.K. Kulovits, C. Liu, K. Zweiacker, B.W. Reed, T. LaGrange, J.M. K. Wiezorek, G.H. Campbell, In situ transmission electron microscopy of crystal growth-mode transitions during rapid solidification of a hypoeutectic Al–Cu alloy, Acta Mater. 65 (2014) 56–68, https://doi.org/10.1016/j.actamat.2013.11.046.
[11] J.T. McKeown, K. Zweiacker, C. Liu, D.R. Coughlin, A.J. Clarke, J.K. Baldwin, J. W. Gibbs, J.D. Roehling, S.D. Imhoff, P.J. Gibbs, D. Tourret, J.M.K. Wiezorek, G. H. Campbell, Time-resolved in situ measurements during rapid alloy solidification: experimental insight for additive manufacturing, JOM. 68 (2016) 985–999, https://doi.org/10.1007/s11837-015-1793-x.
[12] K. Zweiacker, J.T. McKeown, C. Liu, T. LaGrange, B.W. Reed, G.H. Campbell, J.M. K. Wiezorek, Determination of crystal growth rates during rapid solidification of polycrystalline aluminum by nano-scale spatio-temporal resolution in situ transmission electron microscopy, J. Appl. Phys. 120 (2016) 55106, https://doi.org/10.1063/1.4960443.
[13] J.D. Roehling, D.R. Coughlin, J.W. Gibbs, J.K. Baldwin, J.C.E. Mertens, G. H. Campbell, A.J. Clarke, J.T. McKeown, Rapid solidification growth mode transitions in Al-Si alloys by dynamic transmission electron microscopy, Acta Mater. 131 (2017) 22–30, https://doi.org/10.1016/j.actamat.2017.03.061.
[14] K.W. Zweiacker, C. Liu, M.A. Gordillo, J.T. McKeown, G.H. Campbell, J.M. K. Wiezorek, Composition and automated crystal orientation mapping of rapid solidification products in hypoeutectic Al-4 at.%Cu alloys, Acta Mater. 145 (2018) 71–83, https://doi.org/10.1016/j.actamat.2017.11.040.
[15] J.T. McKeown, A.J. Clarke, J.M.K. Wiezorek, Imaging transient solidification behavior, MRS Bull. 45 (2020) 916–926, https://doi.org/10.1557/mrs.2020.273.
[16] V. Bathula, C. Liu, K. Zweiacker, J. McKeown, J.M.K. Wiezorek, Interface velocity dependent solute trapping and phase selection during rapid solidification of laser melted hypo-eutectic Al-11at.%Cu alloy, Acta Mater. 195 (2020) 341–357, https://doi.org/10.1016/j.actamat.2020.04.006.
[17] T. Pinomaa, J.M. McKeown, J.M.K. Wiezorek, N. Provatas, A. Laukkanen, T. Suhonen, Phase field modeling of rapid resolidification of Al-Cu thin films, J. Cryst. Growth 532 (2020), 125418, https://doi.org/10.1016/j.jcrysgro.2019.125418.
[18] P. Jreidini, T. Pinomaa, J.M.K. Wiezorek, J.T. McKeown, A. Laukkanen, N. Provatas, Orientation gradients in rapidly solidified pure aluminum thin films: comparison of experiments and phase-field crystal simulations, Phys. Rev. Lett. 127 (2021), 205701, https://doi.org/10.1103/PhysRevLett.127.205701.
[19] S.C. Gill, W. Kurz, Rapidly solidified AlCu alloys—I. Experimental determination of the microstructure selection map, Acta Metall. Mater. 41 (1993) 3563–3573, https://doi.org/10.1016/0956-7151(93)90237-M.
[20] D. Vaughan, J.M. Silcock, The orientation and shape of θ precipitates formed in an Al–Cu alloy, Phys. Status Solidi 20 (1967) 725–736, https://doi.org/10.1002/pssb.19670200235.
[21] D.A. Porter, K.E. Easterling, M.Y. Sherif, Phase Transformations in Metals and Alloys, Third edit, CRC Press, Florida, USA, 1992.
[22] C.S. Kaira, C. Kantzos, J.J. Williams, V. De Andrade, F. De Carlo, N. Chawla, Microstructural evolution and deformation behavior of Al-Cu alloys: a transmission X-ray Microscopy (TXM) and micropillar compression study, Acta Mater. 144 (2018) 419–431, https://doi.org/10.1016/j.actamat.2017.11.009.
[23] B. Vishwanadh, J.T. McKeown, J.M.K. Wiezorek, HAADF and analytical TEM of the metastable α-Al and θ'-Al2Cu phases in a rapidly solidified hypo-eutectic Al-Cu alloy, Microsc. Microanal. 25 (2019) 1528–1529, https://doi.org/10.1017/S1431927619008377.
[24] J. Mayer, L.A. Giannuzzi, T. Kamino, J. Michael, TEM sample preparation and FIB-induced damage, MRS Bull. 32 (2007) 400–407, https://doi.org/10.1557/mrs2007.63.

[25] D. Kiener, C. Motz, M. Rester, M. Jenko, G. Dehm, FIB damage of Cu and possible consequences for miniaturized mechanical tests, Mater. Sci. Eng. A 459 (2007) 262–272, https://doi.org/10.1016/j.msea.2007.01.046.
[26] K.A. Unocic, M.J. Mills, G.S. Daehn, Effect of gallium focused ion beam milling on preparation of aluminium thin foils, J. Microsc. 240 (2010) 227–238, https://doi.org/10.1111/j.1365-2818.2010.03401.x.
[27] S. Lee, J. Jeong, Y. Kim, S.M. Han, D. Kiener, S.H. Oh, FIB-induced dislocations in Al submicron pillars: annihilation by thermal annealing and effects on deformation behavior, Acta Mater. 110 (2016) 283–294, https://doi.org/10.1016/j.actamat.2016.03.017.
[28] B.A. Benson, R.G. Hoagland, Crack growth behavior of a high strength aluminum alloy during LME by gallium, Scr. Metall. 23 (1989) 1943–1948, https://doi.org/10.1016/0036-9748(89)90487-0.
[29] R. Stumpf, P.J. Feibelman, Towards an understanding of liquid-metal embrittlement: energetics of Ga on Al surfaces, Phys. Rev. B 54 (1996) 5145–5150, https://doi.org/10.1103/PhysRevB.54.5145.
[30] N.I. Kato, Reducing focused ion beam damage to transmission electron microscopy samples, J. Electron Microsc. 53 (2004) 451–458, https://doi.org/10.1093/jmicro/dfh080.
[31] A. Barna, B. Pécz, M. Menyhard, Amorphisation and surface morphology development at low-energy ion milling, Ultramicroscopy. 70 (1998) 161–171, https://doi.org/10.1016/S0304-3991(97)00120-4.
[32] D.J. Barber, Radiation damage in ion-milled specimens: characteristics, effects and methods of damage limitation, Ultramicroscopy. 52 (1993) 101–125, https://doi.org/10.1016/0304-3991(93)90025-S.
[33] Y. Kwon, B.-S. An, Y.-J. Shin, C.-W. Yang, Method of Ga removal from a specimen on a microelectromechanical system-based chip for in-situ transmission electron microscopy, Appl. Microsc. 50 (2020) 22, https://doi.org/10.1186/s42649-020-00043-6.
[34] P.E. Fischione, R.E.A. Williams, A. Genç, H.L. Fraser, R.E. Dunin-Borkowski, M. Luysberg, C.S. Bonifacio, A. Kovács, A small spot, inert gas, ion milling process as a complementary technique to focused ion beam specimen preparation, Microsc. Microanal. 23 (2017) 782–793, https://doi.org/10.1017/S1431927617000514.
[35] T. Malis, S.C. Cheng, R.F. Egerton, EELS log-ratio technique for specimen-thickness measurement in the TEM, J. Electron Microsc. Tech. 8 (1988) 193–200, https://doi.org/10.1002/jemt.1060080206.
[36] K. Iakoubovskii, K. Mitsuishi, Y. Nakayama, K. Furuya, Mean free path of inelastic electron scattering in elemental solids and oxides using transmission electron microscopy: atomic number dependent oscillatory behavior, Phys. Rev. B 77 (2008), 104102, https://doi.org/10.1103/PhysRevB.77.104102.
[37] T.-F. Chung, Y.-L. Yang, C.-N. Hsiao, W.-C. Li, B.-M. Huang, C.-S. Tsao, Z. Shi, J. Lin, P.E. Fischione, T. Ohmura, J.-R. Yang, Morphological evolution of GP zones and nanometer-sized precipitates in the AA2050 aluminium alloy, Int. J. Light. Mater. Manuf. 1 (2018) 142–156, https://doi.org/10.1016/j.ijlmm.2018.06.002.